A hierarchical shell locks and stabilizes perovskite nanocrystals with near-unity quantum yield

Qingsen Zeng[1,2], Yue Zhao[1], Sunghee Park[3, 4], Huanyu Zhou[1], Hyun-Joon Shim[1,5], Tianshu Li[6], Jinseok Ryu[1], Min-Jun Sung[1], Xian Wei Chua[7,8], Eojin Yoon[1], Barney A.I. Lewis[7,8], Seung-Je Woo[1], Michele Forzatti[9], Min Ju Kim[10], Eun A Kim[10,11], Linjie Dai[7,8], Jinhyeong Jang[12,13], Yipeng Tang[14], Jin Jung Kweon[15,16], Hao Chen[1], Kyung Yeon Jang[1], Dong-Hyeok Kim[1], Woo Jin Jeong[1], Joo Sung Kim[1,5], Hyejin Lee[1], Kyueun Lim[1,5], Seong-Yong Cho[10,11], Chan Beum Park[13], Sung Keun Lee[15,16], Miyoung Kim[1], Henk J. Bolink[9], Bin Hu[14], Aron Walsh[6], Samuel D. Stranks[7,8], and Tae-Woo Lee[1,2,4,5,17*]

[1]Department of Materials Science and Engineering, Seoul National University, 1 Gwanak-ro, Gwanak-gu, Seoul 08826, Republic of Korea.
[2]Research Institute of Advanced Materials, Seoul National University, 1 Gwanak-ro, Gwanak-gu, Seoul 08826, Republic of Korea.
[3]PEROLED Inc., Building 940, 1 Gwanak-ro, Gwanak-gu, Seoul 08826, Republic of Korea.
[4]Soft Foundry, Seoul National University, 1 Gwanak-ro, Gwanak-gu, Seoul 08826, Republic of Korea.
[5]SN Display Co. Ltd., Building 35, 1 Gwanak-ro, Gwanak-gu, Seoul 08826, Republic of Korea.
[6]Department of Materials, Imperial College London, London, UK.
[7]Department of Physics, Cavendish Laboratory, University of Cambridge, Cambridge, UK.
[8]Department of Chemical Engineering and Biotechnology, University of Cambridge, Cambridge, UK.
[9]Instituto de Ciencia Molecular (ICMol), Universidad de Valencia, Catedrático José Beltrán, 2, 46980 Paterna, Spain.
[10]Department of Photonics and Nanoelectronics, Hanyang University ERICA, Ansan 15588, Republic of Korea.
[11]HYU-KITECH Joint Department, Hanyang University, Ansan 15588, Republic of Korea.
[12]Department of Materials Science and Engineering, Korea Advanced Institute of Science and Technology (KAIST), 335 Science Road, Daejeon 34141, Republic of Korea.
[13]Applied Science Research Institute, Korea Advanced Institute of Science and Technology (KAIST), 335 Science Road, Daejeon 34141, Republic of Korea.
[14]Department of Materials Science and Engineering, University of Tennessee, Knoxville, TN 37996, USA.
[15]School of Earth and Environmental Sciences, Seoul National University, Seoul 08826, Republic of Korea.
[16]Institute of Applied Physics, Seoul National University, Seoul 08826, Republic of Korea.
[17]Institute of Engineering Research, Interdisciplinary Program in Bioengineering, Seoul National University, Seoul 08826, Republic of Korea.
**Author to whom correspondence should be addressed: E-mail: twlees@snu.ac.kr, taewlees@gmail.com*

Abstract

Solid-state emitters have exhibited external quantum yields (EQYs) below 65%, with no system combining unity photoluminescence quantum yield (PLQY) and commercially viable stability. These limitations are most pronounced in colloidal perovskite nanocrystals (PeNCs), given their soft ionic lattices and labile surfaces. We introduce a hierarchical shell (HS) structure comprising inter-bonded $PbSO_4/SiO_2$/polymer multilayers that simultaneously locks and stabilizes soft lattices and labile interfaces. HS-$CsPbBr_3$ PeNC films exhibit T_{90} (10% PLQY loss) = 3,211 h under accelerated 60 °C/90% relative humidity (RH) and T_{90} = 12,000 h under blue-light exposure. HS strategy generalizes across PeNC compositions, including mixed-halide, mixed-cation, iodide, and hybrid PeNCs, and enables $MAPbBr_3$ with extended T_{90} = 3,900 h (60 °C/90% RH) and T_{90} = 27,234 h (blue light). Moreover, HS-$MAPbBr_3$ films with 100.0% PLQY eliminate self-absorption losses and achieve an EQY of 91.4%, approaching the theoretical maximum. The HS barrier also prevents lead leakage for safety of large-area, high-resolution displays, and bio-optoelectronics.

For nearly a century, luminescent materials have powered advances in displays, lighting, sensing, imaging, and optical communication (*1-5*). Many systems, ranging from rare-earth/transition-metal phosphors, organic semiconductors and quantum dots (QDs) to emerging carbon dots, metal nanoclusters and halide perovskites, have demonstrated photoluminescence quantum yields (PLQYs) > 90% in dilute solution or dispersions (*6-14*). However, such efficiencies are typically realized under low absorptance (A), solution-phase environments, or deep-ultraviolet (UV) excitation (<300 nm), limiting their relevance for solid-state devices excited by commercial light sources (365 to 450 nm).

In practical applications, solid emitters must simultaneously exhibit strong absorption and high PLQY to maximize light-conversion efficiency, as quantified by the external quantum yield (EQY = A × PLQY). This balance is fundamentally constrained by an intrinsic trade-off: as concentration increases to boost absorptance, concentration quenching and nonradiative losses from self-absorption inevitably reduce PLQY (*8-11, 15-17*), limiting EQY to < 65% across nearly all known solid emitters (**Tables S1 to S6**). As a result, > 2,000 TWh of electricity, ~8% of global electricity consumption, is lost annually because of suboptimal electro-optical conversion in lighting and display applications (*18*). In principle, achieving 100% PLQY—such that every photon is emitted, and every reabsorbed photon is re-emitted—would fully mitigate self-absorption losses and allow EQY to approach its theoretical maximum.

Colloidal halide perovskite nanocrystals (PeNCs) have emerged as bright emitters with exceptional color purity, high absorption coefficient, and >95% PLQY in well-passivated solution (*19-22*), offering strong potential for achieving high EQY in solids. However, environmental stressors (such as light, heat, moisture, and oxygen) easily degrade the ionic PeNCs; this reaction severely reduces the PLQY and operational lifetime (*23, 24*). In bulk perovskite crystals, light- or heat-induced lattice expansion and tensile strain have recently been identified as key degradation pathways, which weaken ionic bonding and accelerate ion migration, phase separation, and defect formation (*25-27*).

Colloidal PeNCs surrounded by weakly bound ligands share this intrinsic lattice softness, but the impact of lattice softening–driven degradation in colloidal systems has been largely overlooked. Their degradation is further complicated by labile surface chemistry and direct environmental exposure (*28*), especially under operational conditions where both the lattice and interface undergo dynamic evolution. We propose that degradation in colloidal PeNCs, particularly those lacking strong shell-to-lattice anchoring, is best understood as a lattice–interface interlinked process, in which lattice expansion and softening, and interfacial chemical reactions at labile surface cooperatively accelerate structural and optical deterioration. This mechanistic gap has limited the rational design of stable and efficient PeNC materials.

For practical device integration, solid-state emitters are designed to meet commercial aging benchmarks, typically a time for 10% PLQY loss T_{90} > 1,000 h under 60°C/90% relative humidity (RH) and T_{90} >10,000 h under continuous blue-light irradiation (**Supplementary Note 1**). Existing stabilization strategies of PeNCs, such as polymer encapsulation (*29, 30*), oxide shell coating (*31, 32*), and ligand crosslinking (*33*), remain fundamentally limited, as they generally function as passive diffusion barriers that hinder moisture and oxygen ingress. Relying on weakly bound ammonium or carboxylate surface ligands (*29-33*), all of these methods offer only limited anchoring to the ionic lattice and fail to address degradation pathways arising from lattice-interface interlinked degradation under operational stress. Therefore, these methods struggle to sustain the high PLQY of PeNC films > 80% over commercially viable operational lifetimes (**Table S7**) (*29-33*). Furthermore, no existing strategy is widely applicable across PeNC compositions (such as mixed-halide, organic-inorganic

hybrid, mixed-cation or iodide-rich); this limitation presents a critical challenge, as these more labile formulations are particularly prone to phase separation, halide oxidation, and ion migration under operational conditions *(22, 34)*.

Here, we report a hierarchical shell (HS) structure, composed of an inter-bonded $PbSO_4$, SiO_2, and polymer network, to achieve both high PLQY and commercially viable lifetime in PeNCs. This HS design introduces lattice–interface interlocking as a stabilization strategy that confines the perovskite lattice and locks the surface, which suppress degradation pathways driven by lattice softening, ion migration, and interfacial reactions. HS-$MAPbBr_3$ (MA = methylammonium) films exhibited 100.0% PLQY (average: 98.6%), which minimized nonradiative losses and transforms self-absorption into beneficial photon recycling.

As a result, a 20 wt% film delivered an EQY of 91.4%, approaching the theoretical maximum and surpassing all reported solid emitters (EQY < 65%), including rare-earth phosphors, organics, quantum dots, carbon dots, metal nanoclusters, and halide perovskites. Moreover, HS-$CsPbBr_3$ PeNC films achieved commercially viable photoluminescence stability, with T_{90} = 3,211 h at accelerated 60 °C/90% RH stress and T_{90} =12,000 h under continuous 180 W/m^2 blue-light exposure. This HS strategy was effective across diverse compositions, and notably enables HS-$MAPbBr_3$ to achieve extended humid-thermal and photostability lifetimes, surpassing T_{90} = 3,900 h and estimated T_{90} = 27,234 h, respectively. Finally, we show that HS-PeNCs exhibited no lead leakage and excellent roll-to-roll printability and patterning compatibility, making them well-suited for biocompatible, large-area, high-resolution display applications.

Synthesis of hierarchical shell

The HS structure (**Fig. 1A**) consisted of inter-bonded $PbSO_4$, SiO_2, and siloxane polymer layers, that formed a lattice-interface interlocking network. The inner $PbSO_4$ layer has high lattice energy (~2400 kJ/mol) and directly anchored the perovskite lattice, and effectively locked surface ions and passivates surface trap states *(35)*. The intermediate SiO_2 layer, chemically coupled by 3-triethoxysilylpropylammonium (APTES), reinforced the $PbSO_4$/perovskite interface. The outer siloxane polymer layer was covalently grafted to SiO_2 by Si–O bonds; this arrangement ensured uniform dispersion of PeNCs in siloxane resins and introduced additional spatial confinement and environmental shielding. This chemically interlocked multi-shell system simultaneously modulated lattice dynamics and surface chemistry, thereby forming a unified stable structure that enabled efficient, stable, and solution-processable PeNCs.

HS-$CsPbBr_3$ PeNCs were fabricated using a multi-step process (**Fig. S1**), enabled by the rationally designed $(APTES)_2SO_4$ reagent (**Fig. S2A to C**), which simultaneously achieved surface reconstruction and chemical anchoring. Treatment of $CsPbBr_3$ PeNCs with $(APTES)_2SO_4$ selectively etched away surface CsBr in ⩽ 2 min (**Fig. S2D to E**), to yield a Pb^{2+}-rich termination (**Fig. S3 and S4**). Transmission electron microscopy (TEM) imaging confirmed formation of a $PbSO_4$ monolayer (thickness: ~0.2 nm) rather than bulk deposition (**Fig. S1C** and **S4**), thus avoiding lattice strain (**Fig. S5**). This tailored $PbSO_4$/APTES surface passivated surface defects and boosted PLQY from 46% to 99% in $CsPbBr_3$ solution (**Fig. S2F**), and also provided a chemically reactive surface to anchor the subsequent SiO_2 shells.

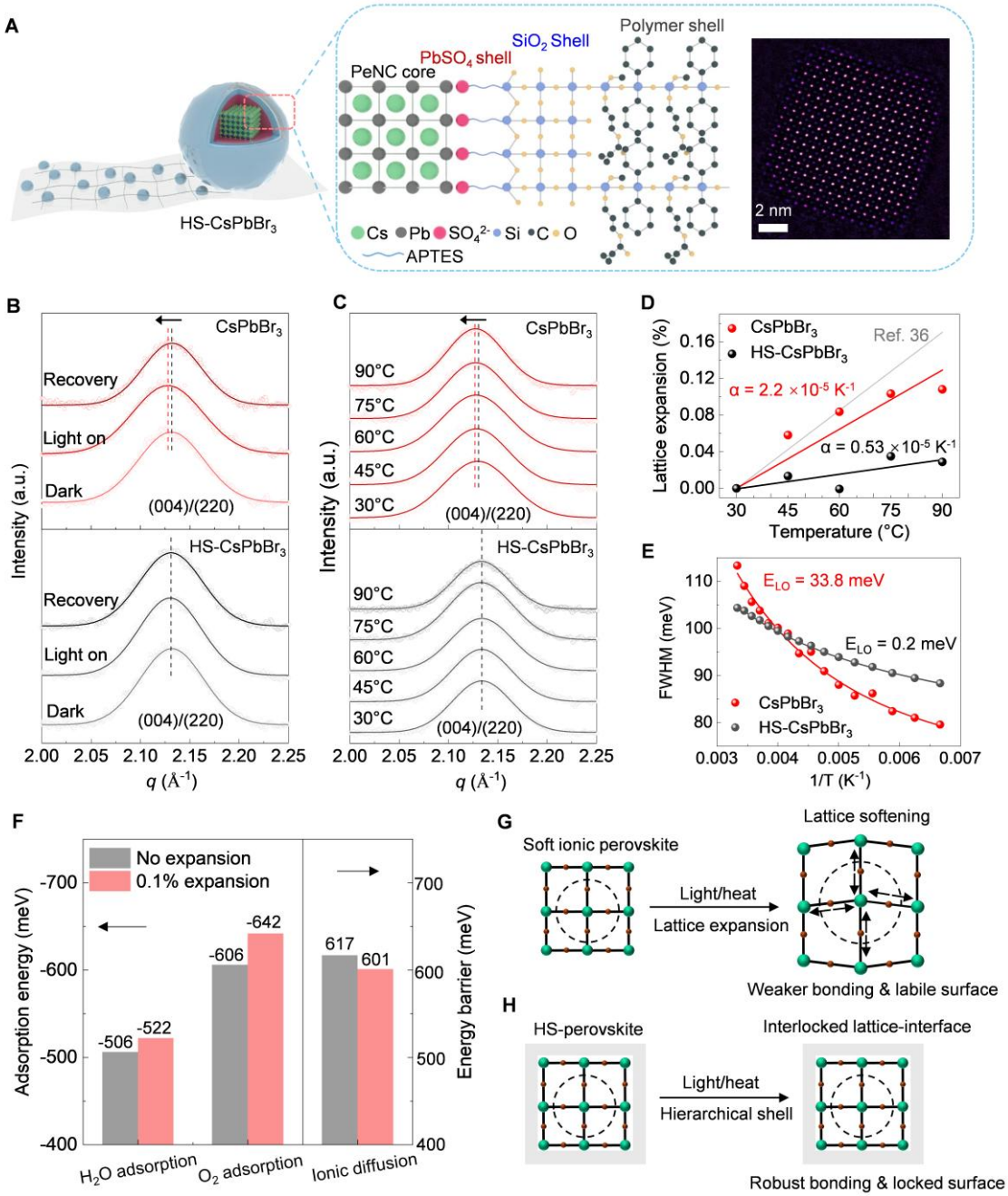

Figure 1 Hierarchical shells confined perovskite lattice. (A) Structure of hierarchical shell. Inset is a high-resolution STEM lattice image of a typical inner $CsPbBr_3$ core. (B and C) Integrated profiles (out of plane) of $CsPbBr_3$ (top) and HS-$CsPbBr_3$ (bottom) obtained from *in situ* light irradiation (B) and heating (C) GIWAXS experiments. (D) Expansion of lattice planes from heating experiments vs temperature, and linear fits. Gray line: reported thermal expansion coefficient of $CsPbBr_3$ PeNCs (*36*). (E) FWHM of PL spectra vs $1/T$ from 150 to 300 K. (F) DFT-calculated adsorption energies (E_{ads}) of H_2O and O_2 molecules and ionic migration barriers on the $CsPbBr_3$ surface under zero strain and 0.1% lattice expansion. A 0.1% lattice expansion was selected because photo/thermal effects were experimentally found to induce ~0.1% strain in $CsPbBr_3$ nanocrystals. (G and H) Scheme of lattice response to heat or light stimulation in bare-PeNCs (G) and HS-PeNCs (H).

After $PbSO_4$/APTES surface reconstruction, the PeNCs were subjected to controlled hydrolysis of tetramethoxysilane (TMOS) under trace water in toluene, to form a conformal SiO_2 layer (thickness:

~2.5 nm, **Fig. S1D** and **S6**). This thin SiO_2 layer covalently bridged to APTES; this process reinforced the perovskite/$PbSO_4$/SiO_2 interface while maintaining the optical and structural integrity of the PeNC cores (**Fig. S6 to S9**). The final step involves blending $CsPbBr_3$/$PbSO_4$/SiO_2 PeNCs with siloxane precursors (diphenylsilanediol (DPSD) and methacryloxypropyltrimethoxysilane (MPTMS)), which underwent *in situ* polymerization to form the siloxane polymer shell (**Fig. S10**). The polymer shell both increased dispersion stability within siloxane resins, and induced crosslinked network confinement around PeNCs. This multi-layered chemical interlocking delivered storage stability > 400 days without measurable PL decay (**Fig. S11**), which is superior to those of conventional PeNC colloids, and makes HS-PeNCs ideally suited for large-scale manufacturing and long-term storage.

The uniform HS-$CsPbBr_3$ resin could be directly processed to form homogeneous thin films by bar-coating (**Fig. S10F and G**). During photo-curing, acrylate crosslinking within the polymer matrix further reinforced the inter-shell mechanical coupling, and thereby formed a mechanically-robust yet optically-transparent network. In solid films, HS-$CsPbBr_3$ retained a remarkably high PLQY of 95.0% (average: 92.0%), versus the PLQY of control bare-$CsPbBr_3$ films (32.0%, average: 30.0%) (**Table S8**). This increase reflected the critical passivation function of lattice-interface interlocked HS in suppressing solid-state nonradiative recombination (**Supplementary Note 2**). Suppressed surface trap-assisted recombination of HS-$CsPbBr_3$ was confirmed by transient photoluminescence (TrPL) and transient absorption (TA) analysis (**Fig. S12 to S14**). Moreover, the HS layer weakened orbit–orbit interactions (**Fig. S15**), and thus effectively prevented bright-to-dark state conversion and enabled high PLQY in PeNC solids.

Lattice-interface interlocking by a hierarchical shell

To test whether lattice softening contributes directly to the acceleration of PeNC degradation, we conducted *in situ* synchrotron grazing-incidence wide-angle x-ray scattering (GIWAXS) to track lattice strain evolution under controlled conditions of illumination or thermal stress (**Fig. S16 to S18**). Both $CsPbBr_3$ PeNC/siloxane film and HS-$CsPbBr_3$ PeNC/siloxane film showed diffraction peaks at q = 1.12, 1.51, and 2.13 $Å^{-1}$, which were indexed to (002)/(110), (112)/(020)/(200), (004)/(220) crystal facets, respectively (**Fig. S17**). Among these, the (004)/(220) plane was selected for strain analysis, because its high diffraction angle and multiplicative factor provided high sensitivity to changes in structural symmetry (*37*).

In bare-$CsPbBr_3$ film, blue-light illumination caused a decrease in the q of the diffraction peak of (004)/(220) (top frame of **Fig. 1B**); this change indicated photoinduced lattice expansion. This shift scaled with incident light intensity, confirming that the expansion was a direct effect of photoexcitation, rather than of cumulative light dose or thermal effects (**Fig. S17**) (*36, 38*). When the illumination ceased, the peak fully returned to its original position; this change demonstrated that the lattice relaxation was reversible. Light-induced lattice expansion generated tensile strain that weakened ionic bonding, leading to lattice softening. In contrast, in HS-$CsPbBr_3$/siloxane films, blue-light illumination had no effect on the q of the diffraction peak of (004)/(220) (bottom frame in **Fig. 1B**). This result confirmed that the hierarchical shell effectively locked the perovskite lattice, and thus suppressed photoinduced tensile strain.

The trends in thermal expansion upon heating from 30 °C to 90 °C were similar to those of photo-illumination. In $CsPbBr_3$ films, this heating decreased the q of the diffraction peaks (top frame of **Fig. 1C**); calculations using this shift indicate a thermal expansion coefficient $\alpha = (2.2 \pm 0.2) \times 10^{-5}\ K^{-1}$, (**Fig. 1D**) which is near reported values for $CsPbBr_3$ PeNCs (*36*). In contrast, HS-$CsPbBr_3$ films

showed almost no thermal expansion (bottom frame of **Fig. 1C**), with $\alpha = (0.53 \pm 0.2) \times 10^{-5}$ K^{-1} (**Fig. 1D**). This comparison confirmed that the HS constrained lattice breathing, and thereby anchored the ionic lattice and increased its mechanical rigidity.

This confined lattice also altered the optical response of HS-$CsPbBr_3$ (**Fig. S19**). Temperature-dependent PL measurements revealed suppressed PL quenching, increased exciton-binding energy (**Fig. S19C**), and an anomalous redshift in the PL peak (**Fig. S19D**); notably, the PL peak evolution shifted from anti-Varshni behavior in bare-$CsPbBr_3$ to Varshni behavior in HS-$CsPbBr_3$, providing strong evidence of lattice locking (**Supplementary Note 3**). Consistent with this lattice stabilization, the fitted longitudinal optical (LO) phonon energy reduced from 33.8 meV in bare-$CsPbBr_3$ to near-zero in HS-$CsPbBr_3$ (**Fig. 1E**), indicating that exciton–phonon coupling was suppressed and lattice dynamics were stabilized.

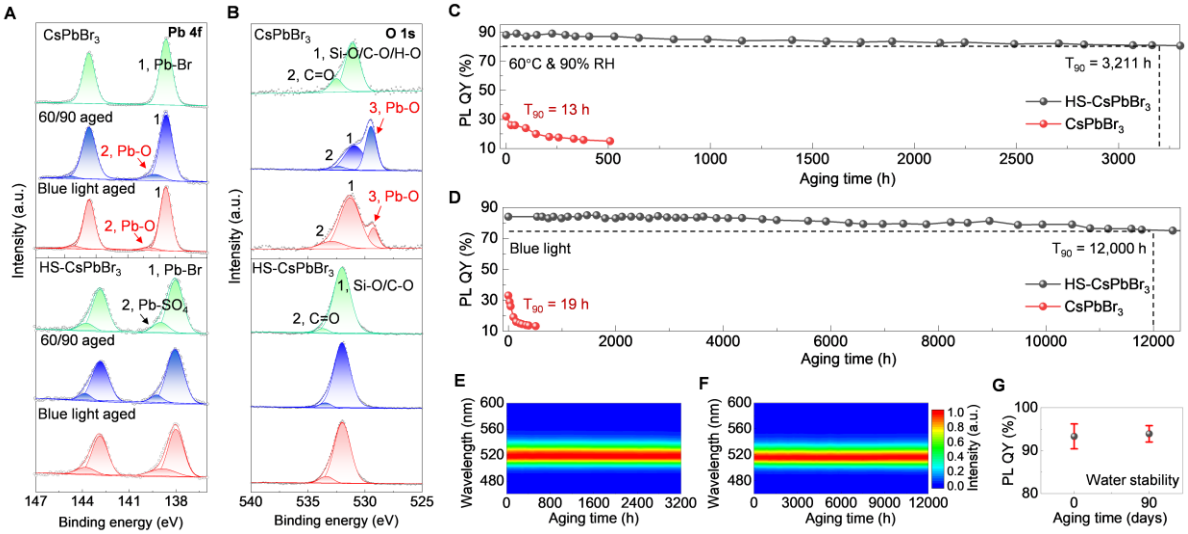

Figure 2 Aging stability of HS-PeNCs. (A) Pb^{4f} and (B) O^{1s} XPS spectra of $CsPbBr_3$ (top) and HS-$CsPbBr_3$ (bottom) films before and after aging under 60 °C/90% RH (denoted as 60/90) and 180 W/m^2 blue-light irradiation. (C and D) Profiles of PLQY over aging time for $CsPbBr_3$ and HS-$CsPbBr_3$ films aging under 60 °C/90% RH (C) and 180 W/m^2 blue light (D). (E and F) Profiles of PL spectra vs aging duration for HS-$CsPbBr_3$ films under 60 °C/90% RH (E) and blue light (F). (G) PLQY record of HS-$CsPbBr_3$ in water.

To understand how lattice expansion influences interfacial stability, we first performed density functional theory (DFT) calculations to study molecular adsorption and ionic migration on $CsPbBr_3$ surfaces. A slight lattice expansion of 0.1% enhanced the adsorption of both H_2O (E_{ads} from –506 to –522 meV; E_{ads}: adsorption energy) and O_2 (E_{ads} from –606 to –642 meV), and lowered the migration barrier for Br ions from 617 to 601 meV (**Fig. 1F and Fig. S20**). These results indicated that photo-/thermal-induced lattice softening not only facilitated surface hydrolysis and oxidation but also accelerated ion migration, providing theoretical support for our proposed lattice–interface interlinked degradation pathway of colloidal PeNCs. To experimentally verify these degradation pathways, we tracked the surface chemistry evolution of $CsPbBr_3$ films during 96 h of aging under 60 °C/90% RH or continuous blue-light exposure using x-ray photoelectron spectroscopy (XPS). In both cases, oxidation and hydrolysis were observed, as evidenced by the emergence of Pb–O and CO_3^{2-} signals in the Pb, O, and C spectra (**Fig. 2, A and B,** and **Fig. S21**). These changes directly indicated Pb–Br bond dissociation, leading to the formation of $Pb(OH)_2$ and $PbCO_3$ (*24*). Notably, the degradation was more

pronounced under 60 °C/90% RH than under blue-light illumination, suggesting the moisture-accelerated surface reactions.

These surface-chemical changes were directly linked to structural and optical degradation of $CsPbBr_3$ PeNCs (**Supplementary Note 4**). Under 60 °C/90% RH (**Fig. S22**), $CsPbBr_3$/siloxane film showed PL redshift and full-width at half-maximum (FWHM) broadening, which indicated defect formation and crystal fusion, whereas under blue-light exposure (**Fig. S23**), the PL showed blueshift and FWHM narrowing, which suggested nanocrystal shrinkage due to photoinduced halide oxidation, as supported by XPS analysis. Transient PL measurements (**Fig. S25 and S26**) showed progressive lifetime reduction and spectral evolution, which corroborated these trends. Consequently, bare-$CsPbBr_3$/polymer films achieved only short T_{90} = 13 h under 60 °C/90% RH and 19 h under blue-light irradiation (**Fig. 2C and D**), whereas bare-$CsPbBr_3$/polymer films remained stable for > 300 h when stored at room temperature in dark ambient conditions. This difference emphasized that photo- and thermal-induced lattice expansion and softening strongly accelerated degradation in humid and oxygen-rich environments.

Collectively, these results provided theoretical and experimental evidence of a lattice softening–driven degradation pathway in $CsPbBr_3$ PeNCs, even when protected by polymer coatings. Under illumination or humid-thermal aging, photo- or thermally induced lattice expansion weakened ionic bonding, thereby softening the ionic lattice and destabilizing the labile surface (**Fig. 1G**). This softening promoted surface oxidation and hydration, and facilitated ion migration, ultimately triggering crystal degradation. These findings reveal that lattice softening is a critical upstream driver that initiates and accelerates both lattice and surface deterioration, giving rise to a lattice–interface interlinked degradation pathway, particularly in colloidal PeNCs with insufficient shell-to-lattice anchoring. This mechanistic insight underscores the need to simultaneously confine the lattice and stabilize the surface to achieve long-term operational stability.

In contrast, HS-$CsPbBr_3$ films maintained unaltered surface chemistry and structural integrity even after 3,000 h under 60 °C/90% RH, and under 4,000 h under continuous blue-light exposure (bottom frame in **Fig. 2, A and B, and Fig. S27**). The corresponding T_{90} reached 3,211 hours under 60 °C/90% RH, while blue-light exposure yielded a photostability lifetime of 12,000 h, or more than 630 times longer than that of bare-$CsPbBr_3$. Throughout these tests, HS-$CsPbBr_3$ preserved stable PL spectra with no peak shift or broadening (**Fig. 2, E and F**), thereby surpassing the commercial benchmark in colloidal $CsPbBr_3$ films (**Table S7**). Additional control samples with incomplete shells ($CsPbBr_3$/$PbSO_4$/siloxane, $CsPbBr_3$/$PbSO_4$/APTES/siloxane, and $CsPbBr_3$/$PbSO_4$/SiO_2/isobornyl acrylate (IBOA)) exhibiting high PLQYs (92%, 93%, and 88%, respectively) by $PbSO_4$ passivation, comparable to that of fully protected HS-$CsPbBr_3$–failed within tens to hundreds of hours. This difference confirmed that complete lattice–interface interlocking using HS is essential for achieving long-term operational stability (**Supplementary Note 4**).

Together, these results demonstrate that the HS achieves robust lattice–interface interlocking, realized as an inter-bonded $PbSO_4$/SiO_2/polymer network that simultaneously confined the mechanically soft lattice and chemically stabilized the reactive surface (**Fig. 1H**). This dual protective role was crucial, as it suppressed the lattice–interface interlinked degradation pathway in which lattice expansion, ion migration, and surface oxidation/hydration mutually accelerate structural and optical degradation. Furthermore, systematic variation of the Pb-salt layer ($Pb(HCOO)_2$, $Pb_2(HPO_3)_2$, $PbSO_4$, $Pb_3(PO_4)_2$) and polymer matrix further established the design principle (**Supplementary Note 5**): divalent Pb-salt shells ($Pb_2(HPO_3)_2$ or $PbSO_4$) were required to form interlocked interfacial layers, with

$PbSO_4$ offering the stronger stabilization, while outer APTES/SiO_2/siloxane layers were indispensable for achieving full lattice–interface locking.

The robust HS protection extends beyond photoluminescence stability. HS-$CsPbBr_3$ maintains nearly constant PLQY after 90 days of immersion in water (**Fig. 2G**), and thereby demonstrates comprehensive interfacial sealing and exceptional water resistance. Furthermore, the HS barrier blocked Pb^{2+} release into water, and thus ensured intrinsic environmental safety. In cytotoxicity tests using C2C12 myoblast cells, HS-$CsPbBr_3$ supported healthy cell proliferation comparable to polystyrene culture plates, and far better than bare or partially protected PeNCs (**Fig. S32**). Together, these findings establish that HS-PeNCs are chemically, structurally, optically, and biologically robust materials, which offer long-term environmental stability for applications in displays, lighting, and bio-optoelectronic sensors.

Broad applicability of hierarchical shell

Emission color of halide PeNCs can be tuned across the visible to near-infrared spectrum by adjusting their composition, $APbX_3$ (A = Cs, MA, FA (formamidinium); X = Cl, Br, I, or their mixtures). However, ensuring long-term optical stability across this compositional space is highly challenging owing to photoinduced halide-phase separation in mixed-halide and -cation systems, to oxidation susceptibility in iodide-rich compositions, and to structural fragility of organic-inorganic hybrids. These composition-dependent degradation pathways have so far precluded the development of a universal strategy that simultaneously increases stability and luminescent efficiency across diverse PeNC compositions.

We systematically applied the lattice-interface interlocking HS strategy to representative lead halide PeNC compositions from all-inorganic, organic-inorganic hybrid, mixed-halide, pure-iodide, and mixed-cation systems. The HS successfully stabilized all of these compositions, to produce composition-tunable PeNC resins and films with precisely-tunable emission wavelengths from 409 to 783 nm (**Fig. 3, A to C**, **and S33**). All HS-PeNC resins formed uniform and aggregation-free solid films (**Fig. 3, C to F**). In both solution and solid states, the HS consistently passivated surface defects, and increased the PLQY in all compositions (**Fig. 3G**, **Table S10**), with pure-bromide and iodide-rich systems achieving near-unity PLQY. These outstanding emissive properties arose from the broad lattice compatibility of the HS structure, which accommodated different halide perovskite compositions without introducing significant interfacial strain (**Supplementary Note 6**).

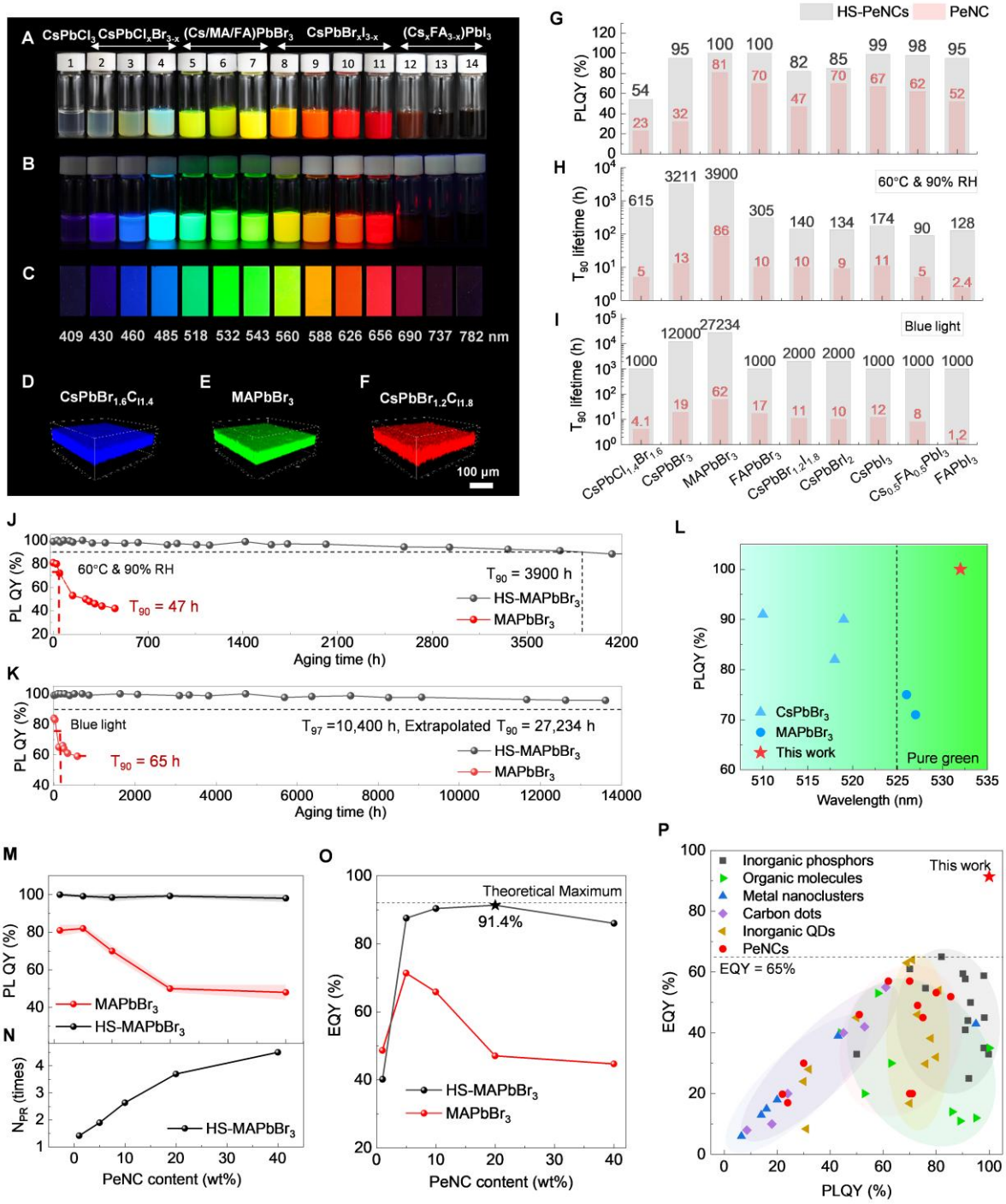

Figure 3 Broad applicability of hierarchical shells. (A to C) Optical image of composition-tunable HS-PeNCs in siloxane resins under daylight (A) and UV light (B), in films under UV light (C). (D to F) PL confocal microscope image of blue (D), green (E) and red (F) HS-PeNC films. (G) PLQY, (H) T_{90} under 60 °C/90% RH (I) T_{90} under 180 W/m^2 blue light of nine typical compositions of bare-PeNCs and HS-PeNCs. (J and K) Profiles of PLQY vs aging duration for $MAPbBr_3$ and HS-$MAPbBr_3$ films under 60 °C/90% RH (J) and blue light (K). In panel K, the T_{90} lifetime is estimated by stretched-exponential fit extrapolation (**Fig. S40**). (L) PLQY vs emission peak for reported colloidal PeNC solid emitters that exhibited high stability under both the 60 °C/90% RH and blue-light exposure conditions, based on data from **Tables S7**. (M) PLQY profiles with increased HS-$MAPbBr_3$ concentrations in 50-μm film, excited at 450 nm. (N) Number of photo-recycling times of HS-

$MAPbBr_3$ vs PeNC concentration. (O) EQY profiles vs PeNC concentration. (P) EQY vs PLQY for various light emitters excited at 365 to 450 nm, based on data from **Tables S1 to S6**.

The HS also consistently extended both humid-thermal and photostability lifetimes, with photostability of all tested compositions increasing by more than two orders of magnitude from several tens of hours to well over 1,000 h (**Fig. 3 H and I**, **S35 to S37, Table S11**). In particular, red-emitting $CsPbBr_{1.2}I_{1.8}$ PeNCs, which typically underwent rapid photoinduced phase separation, had only 11 h of photostability in bare-$CsPbBr_{1.2}I_{1.8}$ films, whereas HS-$CsPbBr_{1.2}I_{1.8}$ retained stable emission and composition for > 2,000 h under continuous blue-light exposure (180 W/m^2). This increase emphasized the effectiveness of HS-mediated lattice anchoring (**Fig. S35**). Similarly, iodide-rich Cs/$FAPbI_3$PeNCs, which had poor phase stability and high susceptibility to photo- and thermo-oxidation, and therefore degraded within ~10 h under humid-thermal and light-aging conditions, but the HS protection increased their humid-thermal lifetimes by > 10 times, and their photostability lifetimes by > 100 times.

Hybrid perovskites such as $MAPbBr_3$ are valued for their Rec. 2020-compatible pure-green emission, but have a softer lattice than inorganic perovskite, and this trait presents additional stabilization challenges. Nevertheless, the HS structure effectively provided lattice-interface interlocking (**Fig. S38 and S39**), and achieved 100.0% PLQY (average: 98.6%). HS-$MAPbBr_3$ films exhibited an extended T_{90} of 3,900 h under 60 °C/90% RH (i.e., 3.9 times the 1,000-h commercial benchmark), and an extrapolated T_{90} of 27,234 h (~37 months) under continuous blue light, 2.7 times the 10,000-h benchmark (**Fig. 3, J and K**, **Fig. S40,** and **Table S12**); these were both immense improvements over control bare-$MAPbBr_3$/siloxane films, which degraded within 86 h under humid-thermal stress and 62 h under continuous blue light. We also demonstrated stable near-unity PLQY in pure-green colloidal PeNC films (525 to 535 nm, **Fig. 3L**, **Table S7**), and surpassed even commercial CdSe/ZnS/polymer QDs in both efficiency and stability (**Fig. S41**).

Moreover, the HS process achieved outstanding batch-to-batch reproducibility, with ten consecutive batches of HS-$MAPbBr_3$ films consistently exceeding commercial aging benchmarks (**Fig. S42**). Collectively, these results established the HS as a universal, compositionally adaptable, and highly reproducible stabilization method that offered robust protection and improved efficiency for lead halide PeNCs of all compositions and emission colors.

Near-unity QY eliminates self-absorption loss

Lead halide PeNCs, including $MAPbBr_3$, exhibited direct band-to-band transitions, large absorption coefficients, and small Stokes shifts *(39)*, which exacerbated self-absorption losses at high concentrations *(17)*. In the bare-$MAPbBr_3$ films, we observed a concentration-dependent PLQY decay from 81% at 1 wt% to 48% at 40 wt% (**Fig. 3M**), highlighting the severity of this issue. In contrast, HS-$MAPbBr_3$ films with 100% PLQY resulted in near-complete suppression of nonradiative recombination and enabling efficient photon recycling. As concentration increased from 1 wt% to 40 wt%, absorptance rose accordingly, accompanied by slight redshifts in PL spectra and prolonged PL lifetimes—signatures of enhanced photon recycling (**Fig. S43 to S44**).

Quantitative modeling (**Supplementary Note 7**) revealed that the average number of photon recycling events (N_{PR}) increased from 1.42 at 1 wt% to 4.49 at 40 wt% (**Fig. 3N**), while the corresponding photon recycling efficiency (η_{PR}) increased from 0.267 to 0.777 (**Table S13**). These effects were fundamentally enabled by the near-unity PLQY, which ensured that nearly all reabsorbed

photons were re-emitted rather than lost to nonradiative decay. Thus, self-absorption was transformed from a loss mechanism into a photon reuse pathway, allowing light to be recycled multiple times before escaping the film. Additionally, HS-$MAPbBr_3$ PeNCs enhanced light scattering within the siloxane film (**Supplementary Note 8**), thereby mitigating optical losses from waveguided modes and improving light outcoupling. As a result, PLQY remained exceptionally high across the entire concentration range, decreasing only slightly from 100.0% at 1 wt% to 98.1% at 40 wt% (**Fig. 3M, and Fig. S45**), with corresponding internal PLQY consistently above 99.6% (**Table S13**). This quenching-resistant process validated the reliability of near-unity PLQY in HS-$MAPbBr_3$ films (**Fig. S46**).

Accordingly, the 20 wt% HS-$MAPbBr_3$ film achieved an EQY of 91.4% (**Fig. 3O**), approaching the theoretical maximum of 92.0% for $MAPbBr_3$/siloxane composites (**Supplementary Note 9**) and surpassing all previously reported solid emitters, including rare-earth/transition metal phosphors, organic emitters, quantum dots, carbon dots, metal nanoclusters, and other halide perovskites excited in the range of commercial light sources (365 to 450 nm) (**Fig. 3P, Table S1 to S6**). This quenching resistance also translated to exceptional device performance, achieving a record color-conversion efficiency of 69.6% versus a previously reported value of 52%, with near-zero blue leakage when applied onto blue LEDs (**Fig. S49 and S50**, **Supplementary Note 10**). Together, these results established HS-PeNCs as a new class of quenching-resistant, high-efficiency, and stable emitters, ideal for next-generation color-conversion displays, solid-state lighting, solar concentrators, and scintillators.

Processability and applications of HS-PeNCs

Colloidal PeNCs have excellent solution processability, but during solid-state deposition their unstable surface ligands often lead to defects and aggregation, which degrade optical characteristics and limit the scalability of fabrication. In contrast, HS-PeNCs, stably dispersed in siloxane resins, displayed remarkable processability and long-term colloidal stability, which facilitated high-quality film formation across various processing platforms. Large-area uniform green and red PeNC/polymer films were fabricated using roll-to-roll printing (**Fig. 4A**, **S51**). Scalable and uniform PeNC patterning was achieved using inkjet printing (**Fig. S52**). Micro-patterns down to 3 μm (pixel density: 3522 pixels per inch (PPI)), meeting the required resolution of micro-LED displays for augmented reality (AR) and virtual reality (VR) applications, can be achieved using high-resolution photolithography (**Fig. 4B**, **S53**).

Compared to previously reported stabilization strategies on colloidal PeNCs, the HS offers a comprehensive improvement in five essential attributes: PLQY, stability, compositional adaptability (universality), cytotoxicity, and processability (**Fig. 4C**, **Table S7**). To demonstrate industrial scalability, we fabricated 4K prototype display panels (3840 × 2160 pixels) by incorporating green HS-$MAPbBr_3$ PeNCs into color-conversion films (**Fig. 4D to F**). The incorporation of HS-$MAPbBr_3$ PeNCs broadened the display's color gamut coverage (**Fig. 4D**) and enhanced imaging quality (**Fig. 4E**). By exploiting the excellent compatibility of HS-PeNCs with standard display processing, we fabricated prototype 10.1-inch tablets, 28-inch and 32-inch monitors, and 43-inch and 75-inch televisions, all demonstrating uniform brightness and vivid color rendering (**Fig. 4F**, **Supplementary Movie S1 to S5**). These displays achieved color-gamut area ratio > 97% of Rec. 2020, 131% of NTSC, and 185% of sRGB (**Table S16**), which exceeded those of commercialized LCDs, InP QDs, and OLED tablets/monitors (**Fig. S54 and S55**). This exceptional color gamut coverage originated from the narrowband and highly efficient pure-green emission of HS-$MAPbBr_3$.

Besides the display applications, flexible HS-PeNC films also show strong potential as light sources for wearable biomedical sensors, owing to combined high lead retention, structural robustness, and composition-tunable, narrowband red-to-NIR emission. These attributes make HS-PeNCs particularly suitable for photoplethysmography or other bio-optoelectronic applications (**Fig. S56, Supplementary Note 11**).

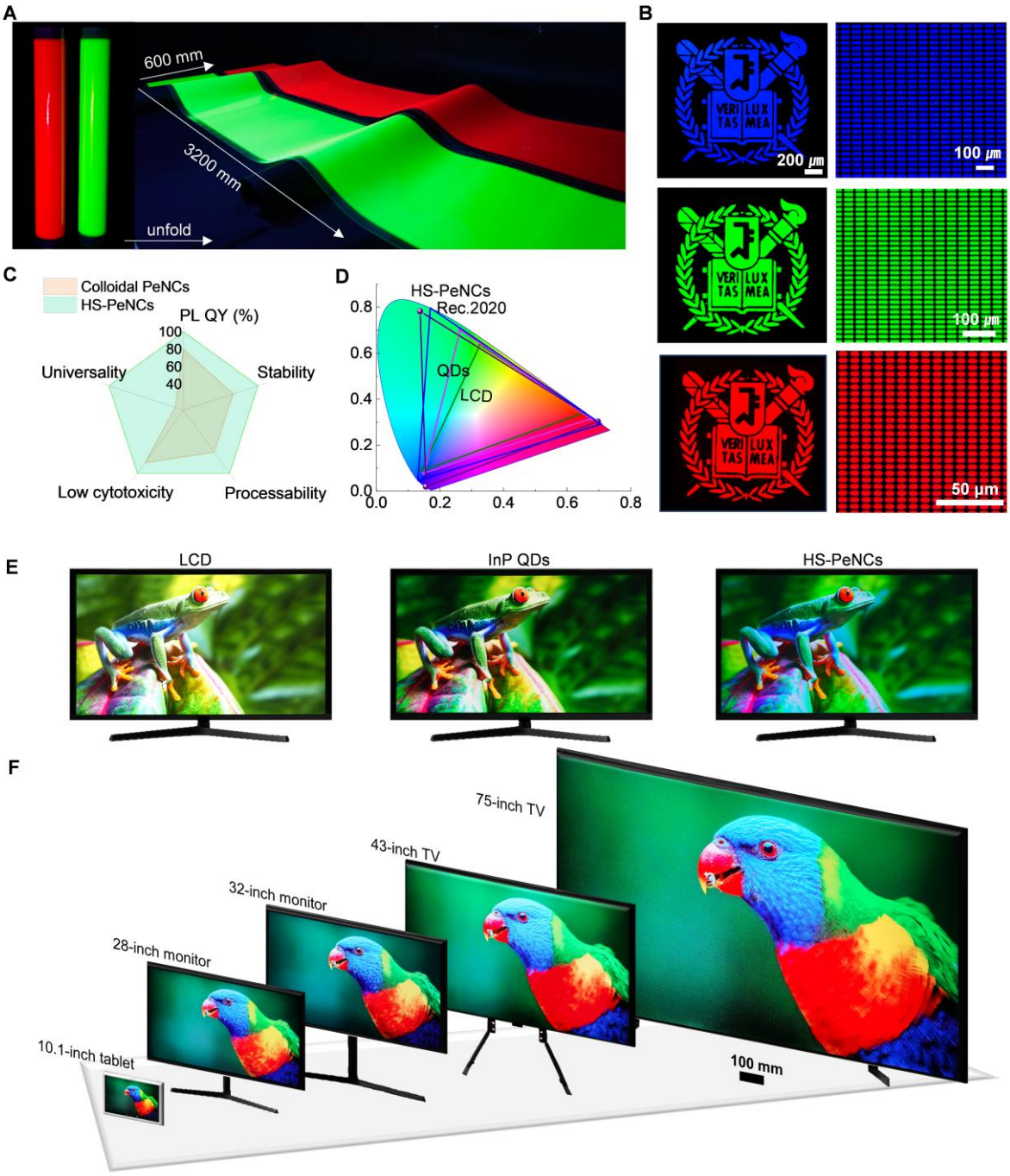

Figure 4 Processability and display applications of HS-PeNCs. (A) Optical images (under UV light) of large-area flexible green HS-$MAPbBr_3$ and red HS-$CsPbBr_{1.2}I_{1.8}$ PeNC films obtained by roll-to-roll printing. (B) The Seoul National University emblem and rectangular micropatterns with varying sizes fabricated by photolithography on HS-PeNC films. Rectangular pixels and their corresponding resolutions are 50 × 20 μm (405 PPI), 30 × 10 μm (667 PPI), and 6 × 3 μm (3522 PPI) for blue, green, and red micropatterns, respectively. (C)

Comparison of performance criteria of HS-PeNCs with other reported fabrication methods in colloidal PeNCs (**Table S7)**. (D) Color gamut coverage of HS-PeNCs compared to commercialized liquid crystal display (LCD) and InP QDs. (E) Display panels (28-inch) incorporating LCD, InP QDs, and HS-PeNCs. (F) Prototype demonstrations of various-size displays that used HS-PeNCs.

Conclusion

We develop a lattice–interface interlocking stabilization strategy, which uses a hierarchical shell (HS) architecture with inter-bonded $PbSO_4/SiO_2$/polymer layers to achieve both high PLQY and commercially viable lifetime in colloidal PeNC solids. This approach minimizes the root cause of PeNC instability, a lattice-interface interlinked degradation pathway, where lattice softening and surface reaction cooperatively accelerate structural and optical deterioration. Mechanistically, the lattice–interface interlocking HS simultaneously locks the soft lattice and stabilizes the surface, suppressing light- or heat-induced expansion and surface reaction, thereby preserving optical performance under stress. As a result, HS-$MAPbBr_3$ films retain 100.0% PLQY (average: 98.6%) and exhibit exceptional stability, with T_{90} = 3,900 h at 60 °C/90% RH and 27,234 h under continuous blue-light exposure, surpassing commercial benchmarks.

Such high PLQY transforms self-absorption into beneficial photon recycling, and thus overcomes the absorptance–PLQY trade-off in various solid emitters, delivering an EQY of 91.4%, close to the theoretical maximum. HS-PeNCs exhibit no lead leakage and are compatible with roll-to-roll printing and high-resolution patterning, making them viable for scalable, high-resolution display technologies. Moreover, the HS strategy generalizes across diverse PeNC compositions, including mixed-halide, mixed-cation, iodide, and organic-inorganic hybrid systems, enabling long-lifetime, color-stable emission across the visible-to-NIR spectrum. More broadly, this lattice–interface interlocking concept offers a transferable design principle for stabilizing soft halide perovskite materials and optoelectronics, which has long been hampered by insufficient operational lifetime.

Materials and methods

Chemicals

3-Aminopropyltriethoxysilane (APTES, 99%), sulfuric acid (99.999%), cesium carbonate (Cs_2CO_3, 99.9%), oleic acid (OA, technical grade 90%), oleylamine (OAm, technical grade 70%), 1-octadecene (ODE, technical grade 90%), $PbBr_2$ (98%), $PbCl_2$ (99%), toluene (anhydrous), methyl acetate (MeOAc, anhydrous), *N,N*-dimethylformamide (DMF) (99.8%), isopropanol (IPA, anhydrous), tetramethoxysilane (TMOS, 99%), barium hydroxide monohydrate, 2,2-dimethoxy-2-phenylacetophenone (BDK), phenylbis(2,4,6-trimethylbenzoyl)phosphine oxide (Irgacure 819), diphenyl(2,4,6-trimethylbenzoyl)phosphine oxide (TPO), formic acid (HCOOH, 98%), trioctylphosphine (TOP), phosphoric acid (H_3PO_4, 99.99%) and phosphorous acid (H_3PO_3, 99%) were purchased from Sigma-Aldrich. Lead(II) iodide (PbI_2, 99.9985%) and *n*-decylamine were purchased from Alfa Aesar. FABr, MABr, and FAI were purchased from Dyesol Ltd. Diphenylsilanediol (DPSD), 3-methacryloxypropyltrimethoxysilane (MPTMS), and 2-isopropylthioxanthone (ITX) were purchased from TCI. 1-Butanol was purchased from Samchun. Polymer-ligand-capped CdSe/ZnS quantum dots were purchased from Dong-A Carbon Tech. All chemicals were used without further purification.

Synthesis of $(APTES)_2SO_4$ and its solutions

$(APTES)_2SO_4$ was prepared by reacting 0.8 mmol APTES with 0.4 mmol of H_2SO_4 in anhydrous IPA. The $(APTES)_2SO_4$ solid was obtained by drying the reaction mixture in a vacuum oven and used for further characterization. To prepare $(APTES)_2SO_4$ solution for growing core-shell PeNCs, 0.4 mmol of $(APTES)_2SO_4$ was dispersed in a mixed solvent composed of 9.5 mL of toluene, 0.5 mL of anhydrous isopropanol, and 0.2 mL of oleic acid (pre-dried at 120 °C for 1 h under reduced pressure). The APTES-HCOO, $(APTES)_2HPO_3$, and $(APTES)_3PO_4$ complexes were synthesized following the same procedure as $(APTES)_2SO_4$, except that H_2SO_4 was replaced with HCOOH, H_3PO_3, and H_3PO_4, respectively.

Synthesis of $CsPbBr_3$ PeNC cores

50 mL of ODE, 5 mL of oleic acid and 5 mL of oleylamine and 800 mg of $PbBr_2$ were loaded into a 250-mL three-necked flask, degassed and dried at 120 °C for 1 h under vacuum. Then the temperature was elevated to 210 °C, and 8 mL of Cs-oleate precursor (0.125 M in ODE) was quickly injected under N_2 atmosphere. After 10 s, the solution was quenched in an ice–water bath, then the $CsPbBr_3$ PeNCs were precipitated by adding MeOAc at an ODE:MeOAc volume ratio of 1:2 and centrifuged at 7,200 rpm for 3 min. The precipitate was redispersed in 18 mL of toluene, precipitated by adding 18 mL of MeOAc, and centrifuged again at 7,200 rpm for 3 min. Finally, $CsPbBr_3$ PeNCs were dispersed in toluene to coat them with a hierarchical shell. All purification steps were performed in air.

Synthesis of $CsPbBr_3/PbSO_4/SiO_2$ double-shell PeNCs

First, 218 mg of $CsPbBr_3$ were dispensed into a 100 mL vial and dispersed in 87.2 mL of anhydrous toluene to form a solution with a concentration of 2.5 mg/mL. Then 4.41 mL of $(APTES)_2SO_4$ solution was added, and the mixture was stirred for 12 h. To grow the SiO_2 shell, 105 µL of TMOS was added in three steps: first, 17.5 µL of TMOS, then 35 µL of TMOS after 1 h, and then 51.5 µL of TMOS after another 1 h. The vial was heated at 30 °C on a hot plate and exposed to air (50–75% relative humidity) to facilitate hydrolysis of TMOS and formation of the SiO_2 shell.

Preparation of hierarchical-shell (HS) $CsPbBr_3$ siloxane resins and films

HS-$CsPbBr_3$ siloxane resins were formed by an *in situ* sol-gel reaction of MPTMS and DPSD (1:1 molar ratio) in the presence of $CsPbBr_3/PbSO_4/SiO_2$ double-shell PeNCs. In this process, the hydroxyl groups (–Si–OH) in DPSD enable the sol–gel reactions (condensation reactions between the hydroxyl group of DPSD and the methoxy group of MPTMS to form Si-O-Si bonds) without additional water (*29*). Barium hydroxide monohydrate was added as a base catalyst to promote the sol-gel reaction. The mixture of PeNCs and silane precursors were held at 80 °C under vacuum for 8 h. Photo-initiators (2 wt%) were added to the HS-$CsPbBr_3$ siloxane resin prior to UV curing. Films were prepared by bar-coating onto PET and UV-curing at 100 mW/cm^2 for 3 min. Unless otherwise noted, characterizations and aging tests were performed on 100 µm-thick films.

The HS-$CsPbBr_3$ siloxane resins and films employing $Pb(HCOO)_2$, $Pb_2(HPO_3)_2$, and $Pb_3(PO_4)_2$ shells were prepared identically, substituting APTES-HCOO, $(APTES)_2HPO_3$, or $(APTES)_3PO_4$ for $(APTES)_2SO_4$, respectively.

Yield of HS-PeNCs

The multi-step HS synthesis maintained high material yield. During $PbSO_4/SiO_2$ deposition, no detectable degradation of PeNCs was observed, and the resulting double-shelled $CsPbBr_3/PbSO_4/SiO_2$

nanocrystals were fully recovered by centrifugation, with yields approaching 100%. In the subsequent in situ polymerization using DPSD and MPTMS, material loss (~25%) was attributed to precursor adhesion to the reaction vessel. For example, starting from 13.3 g of precursors (7.1 g MPTMS and 6.2 g DPSD), ~10 g of HS-PeNC/siloxane composite was obtained, corresponding to an overall synthetic yield of ~75%.

Synthesis of $CsPbX_3$ (X = Cl, Br, I or their mixtures) PeNCs

$CsPbX_3$ PeNCs were synthesized following the synthetic route towards $CsPbBr_3$ PeNCs, except that the precursors were changed as follows: $CsPbCl_3$ (606 mg $PbCl_2$, 5 mL TOP); $CsPbCl_2Br$ (444 mg $PbCl_2$, 213 mg $PbBr_2$); $CsPbCl_{1.4}Br_{1.6}$ (293 mg $PbCl_2$, 413 mg of $PbBr_2$); $CsPbClBr_2$ (182 mg $PbCl_2$, 560 mg $PbBr_2$); $CsPbBr_2I$ (533 mg $PbBr_2$, 333 mg PbI_2); $CsPbBr_{1.7}I_{1.3}$ (453 mg $PbBr_2$, 433 mg PbI_2); $CsPbBr_{1.2}I_{1.8}$ (320 mg $PbBr_2$, 600 mg PbI_2); $CsPbBrI_2$ (266 mg $PbBr_2$, 668 mg PbI_2); $CsPbI_3$ PeNCs (1,000 mg PbI_2). The purification procedure for $CsPbX_3$ PeNCs was the same as for $CsPbBr_3$ PeNCs.

Synthesis of $MAPbBr_3$ and $FAPbBr_3$ PeNCs

$MAPbBr_3$ PeNCs were synthesized in air at room temperature based on the reported protocol (*40*). $MAPbBr_3$ precursor solutions were prepared by dissolving 0.2 mmol of MABr and 0.1 mmol of $PbBr_2$ in 0.5 mL of DMF. Then 0.15 mL of precursor solution was injected into a crystallization-inducing solution that was composed of 0.02 mL of *n*-decylamine, 0.3 mL of oleic acid, 2 mL of 1-butanol and 5 mL of toluene. The reaction was complete after 10 min of vigorous stirring. The resulting colloidal PeNCs were collected by sequential centrifugation at 12,000 rpm for 10 min, and then dispersed in toluene. The reaction could be scaled up to 600 times for mass production (total volume was ~4,440 mL).

$FAPbBr_3$ PeNCs were prepared using the same procedure, except that FABr replaced the MABr precursor.

Synthesis of $FAPbI_3$ PeNCs

$FAPbI_3$ PeNCs were synthesized in air at room temperature. $FAPbI_3$ precursor solutions were prepared by dissolving 0.1 mmol of FAI, 0.05 mmol of PbI_2, 0.6 mL of oleic acid, and 100 μL of oleylamine in 0.5 mL of DMF. Then 0.3 mL of precursor solution was injected into 10 mL of chloroform solution, and reaction was complete after 1 min of vigorous stirring. The colloidal PeNCs with desired size were collected by adding 0.5 mL of acetonitrile and sequential centrifugation at 7,200 rpm for 3 min, and then dispersed in toluene.

Synthesis of $Cs_{0.5}FA_{0.5}PbI_3$ PeNCs

$Cs_{0.5}FA_{0.5}PbI_3$ PeNCs were synthesized using cation-exchange: 17 mg of $FAPbI_3$ and 21.6 mg of $CsPbI_3$ were mixed in a toluene solution that contained 5 μL of OA and 3 μL of OAm. The reaction was complete after stirring for 30 min. MeOAc (twice the total volume of the PeNCs suspension) was added to precipitate the PeNCs. The powders were dispersed in toluene, then centrifuged at 4,000 rpm for 5 min to collect the supernatant.

Synthesis of color- and composition-tunable HS-$APbX_3$ (A = Cs, MA or FA and X = Cl, Br, I or their mixtures) siloxane resins and films

Color- and composition-tunable HS-$APbX_3$ resins and films were prepared using the same procedure

that was used to synthesize HS-$CsPbBr_3$ resin and film, except that different PeNCs were used.

Monitoring aging stability of HS-PeNC films

Films were aged in a humid-thermal chamber (60 °C/90% RH), immersed in water, or irradiated with blue light (180 W/m^2). For blue-light aging, films were positioned 1 cm from the LEDs. Samples were periodically removed for PLQY and spectral measurements using a JASCO FP-8500 spectrofluorometer. No additional encapsulation was used during aging.

Summary of Supplementary Materials

Additional experimental details are provided in the Supplementary Materials, including synthesis of PeNC cores and hierarchical shells, preparation of siloxane composites and films, and device fabrication and characterization methods. Figures S1 to S56 and Tables S1 to S16 present extended structural, optical, and stability analyses, along with benchmarking of solid-state emitters. Supplementary Notes 1 to 11 offer further mechanistic discussion and theoretical modeling. References 40 to 113 list additional literature cited. Supplementary Movies S1 to S5 show display demonstrations enabled by HS-PeNC films.

References

1. H. W. Leverenz, Luminescent solids (phosphors). *Science* **109**, 183-195 (1949).
2. S. Liu *et al.*, Direct Observation of Circularly Polarized Nonlinear Optical Activities in Chiral Hybrid Lead Halides. *J Am Chem Soc* **146**, 11835-11844 (2024).
3. L. Wang *et al.*, Efficient perovskite LEDs with tailored atomic layer number emission at fixed wavelengths. *Science Advances* **11**, eadp9595 (2025).
4. Y. Gao *et al.*, Highly efficient blue light-emitting diodes based on mixed-halide perovskites with reduced chlorine defects. *Science Advances* **10**, eado5645 (2024).
5. X. Lin *et al.*, Electrically-driven single-photon sources based on colloidal quantum dots with near-optimal antibunching at room temperature. *Nat Commun* **8**, 1132 (2017).
6. X. Sun *et al.*, Diffusion-mediated synthesis of high-quality organic–inorganic hybrid perovskite nanocrystals. *Nature Synthesis* **3**, 1-10 (2024).
7. C. Zhu *et al.*, Supramolecular assembly of blue and green halide perovskites with near-unity photoluminescence. *Science* **383**, 86-93 (2024).
8. H. Zhu *et al.*, Highly efficient non-rare-earth red emitting phosphor for warm white light-emitting diodes. *Nat Commun* **5**, 4312 (2014).
9. Y. Khan *et al.*, Synthesis of fluorescent organic nano-dots and their application as efficient color conversion layers. *Nat Commun* **13**, 1801 (2022).
10. S. Zhu *et al.*, Highly photoluminescent carbon dots for multicolor patterning, sensors, and bioimaging. *Angew Chem Int Ed* **52**, 3953-3957 (2013).
11. Z. Han *et al.*, Ultrastable atomically precise chiral silver clusters with more than 95% quantum efficiency. *Sci Adv* **6**, eaay0107 (2020).
12. D. A. Hanifi *et al.*, Redefining near-unity luminescence in quantum dots with photothermal threshold quantum yield. *Science* **363**, 1199-1202 (2019).
13. T. J. Milstein, D. M. Kroupa, D. R. Gamelin, Picosecond Quantum Cutting Generates Photoluminescence Quantum Yields Over 100% in Ytterbium-Doped CsPbCl(3) Nanocrystals. *Nano Lett* **18**, 3792-3799 (2018).
14. D. Zhou *et al.*, Impact of Host Composition, Codoping, or Tridoping on Quantum-Cutting Emission of Ytterbium in Halide Perovskite Quantum Dots and Solar Cell Applications. *Nano Lett* **19**, 6904-6913 (2019).
15. T. Gong *et al.*, Quantum Dot Luminescence Microspheres Enable Ultra-Efficient and Bright Micro-LEDs. *Adv Mater* **37**, e2411999 (2025).
16. C. Kang *et al.*, Quantum-Rod On-Chip LEDs for Display Backlights with Efficacy of 149 lm W^{-1}: A Step toward 200 lm W^{-1}. *Adv Mater* **33**, e2104685 (2021).
17. J. Lin *et al.*, Perovskite Quantum Dots Glasses Based Backlit Displays. *ACS Energy Lett* **6**, 519-528 (2021).
18. IEA, World Energy Outlook 2023; IEA, Energy Efficiency 2022; UNEP, U4E Lighting Report 2023; NRDC, Slashing Energy Use in Televisions, 2019.
19. Y.-H. Kim *et al.*, Comprehensive defect suppression in perovskite nanocrystals for high-efficiency light-emitting diodes. *Nat Photon* **15**, 148-155 (2021).
20. H. Utzat *et al.*, Coherent single-photon emission from colloidal lead halide perovskite quantum dots. *Science* **363**, 1068-1072 (2019).
21. L. Protesescu *et al.*, Nanocrystals of Cesium Lead Halide Perovskites ($CsPbX_3$, X = Cl, Br, and I): Novel Optoelectronic Materials Showing Bright Emission with Wide Color Gamut. *Nano Lett* **15**, 3692-3696

(2015).
22. M. V. Kovalenko, L. Protesescu, M. I. Bodnarchuk, Properties and potential optoelectronic applications of lead halide perovskite nanocrystals. *Science* **358**, 745-750 (2017).
23. D. H. Kim *et al.*, Surface-binding molecular multipods strengthen the halide perovskite lattice and boost luminescence. *Nat Commun* **15**, 6245 (2024).
24. S. Huang *et al.*, Morphology Evolution and Degradation of $CsPbBr_3$ Nanocrystals under Blue Light-Emitting Diode Illumination. *ACS Appl Mater Interfaces* **9**, 7249-7258 (2017).
25. Y. Shen *et al.*, Strain regulation retards natural operation decay of perovskite solar cells. *Nature* **635**, 882-889 (2024).
26. L. A. Muscarella *et al.*, Lattice Compression Increases the Activation Barrier for Phase Segregation in Mixed-Halide Perovskites. *ACS Energy Lett* **5**, 3152-3158 (2020).
27. Y. Z. Qing Li, Haonan Wang, Xinyi Liu, Miaoyu Lin, Xinyuan Sui, Xuesong Leng, Da Liu,, M. S. Zhanpeng Wei, Dongdong Li, Hua Gui Yang, Shuang Yang, Yu Hou, Graphene-polymer reinforcement of perovskite lattices for durable solar cells. *Science* **387**, 1069–1077 (2025).
28. J. De Roo *et al.*, Highly dynamic ligand binding and light absorption coefficient of cesium lead bromide perovskite nanocrystals. *ACS nano* **10**, 2071-2081 (2016).
29. J. Jang *et al.*, Extremely Stable Luminescent Crosslinked Perovskite Nanoparticles under Harsh Environments over 1.5 Years. *Adv Mater* **33**, e2005255 (2021).
30. Q. Pan *et al.*, Ultrahigh Stability of Perovskite Nanocrystals by Using Semiconducting Molecular Species for Displays. *ACS Nano* **16**, 12253-12261 (2022).
31. Z. Li, L. Kong, S. Huang, L. Li, Highly Luminescent and Ultrastable $CsPbBr_3$ Perovskite Quantum Dots Incorporated into a Silica/Alumina Monolith. *Angew Chem Int Ed* **56**, 8134-8138 (2017).
32. S. Wang *et al.*, Organic polystyrene and inorganic silica double shell protected lead halide perovskite nanocrystals with high emission efficiency and superior stability. *Nano Research* **16**, 10507-10514 (2023).
33. Y. Shin *et al.*, Environmentally stable luminescent perovskite nanocrystals passivated and encapsulated by siloxane hybrids enabling reliable color-converted organic light-emitting diodes. *Chem Eng J* **474**, 145889 (2023).
34. Q. A. Akkerman, G. Rainò, M. V. Kovalenko, L. Manna, Genesis, challenges and opportunities for colloidal lead halide perovskite nanocrystals. *Nat Mater* **17**, 394-405 (2018).
35. S. Yang *et al.*, Stabilizing halide perovskite surfaces for solar cell operation with wide-bandgap lead oxysalts. *Science* **365**, 473-478 (2019).
36. M. S. Kirschner *et al.*, Photoinduced, reversible phase transitions in all-inorganic perovskite nanocrystals. *Nat Commun* **10**, 504 (2019).
37. N. Yang *et al.*, An in situ cross-linked 1D/3D perovskite heterostructure improves the stability of hybrid perovskite solar cells for over 3000 h operation. *Energy Environ Sci* **13**, 4344-4352 (2020).
38. H. Tsai *et al.*, Light-induced lattice expansion leads to high-efficiency perovskite solar cells. *Science* **360**, 67-70 (2018).
39. B. Zhao *et al.*, Light management for perovskite light-emitting diodes. *Nat Nanotechnol* **18**, 981-992 (2023).
40. H. M. Jang, S. H. Lee, K. Y. Jang et al., Semi-empirical approach to assess externally-induced photoluminescence linewidth broadening of halide perovskite nanocrystals with particle-size distribution. Commun Phys **6**, 372 (2023).
41. Y. Y. Kim, J. Kim, N. Kim, pGIXS: PLS-II 3C SAXS beamline data plot program with MATLAB.

Zenodo, 10.5281/zenodo.7042272 (2022).

42. B. H. Savitzky *et al.*, Image registration of low signal-to-noise cryo-STEM data. *Ultramicroscopy* **191**, 56-65 (2018).
43. J. Mun *et al.*, In Situ Cryogenic HAADF-STEM Observation of Spontaneous Transition of Ferroelectric Polarization Domain Structures at Low Temperatures. *Nano Lett* **21**, 8679-8686 (2021).
44. J. Jang, C. B. Park, Magnetoelectric dissociation of Alzheimer's β-amyloid aggregates. *Science Advances* **8**, eabn1675 (2022).
45. G. Kresse, J. Hafner, Ab initio molecular dynamics for liquid metals. *Physical review B* **47**, 558 (1993).
46. G. Kresse, J. Furthmüller, Efficiency of ab-initio total energy calculations for metals and semiconductors using a plane-wave basis set. *Computational materials science* **6**, 15-50 (1996).
47. G. Kresse, J. Furthmüller, Efficient iterative schemes for ab initio total-energy calculations using a plane-wave basis set. *Physical review B* **54**, 11169 (1996).
48. S. Grimme, S. Ehrlich, L. Goerigk, Effect of the damping function in dispersion corrected density functional theory. *Journal of computational chemistry* **32**, 1456-1465 (2011).
49. S. Grimme, J. Antony, S. Ehrlich, H. Krieg, A consistent and accurate ab initio parametrization of density functional dispersion correction (DFT-D) for the 94 elements H-Pu. *The Journal of chemical physics* **132**, (2010).
50. P. E. Blöchl, Projector augmented-wave method. *Physical review B* **50**, 17953 (1994).
51. J. Yin *et al.*, Luminescence and stability enhancement of inorganic perovskite nanocrystals via selective surface ligand binding. *ACS nano* **15**, 17998-18005 (2021).
52. S. P. Ong *et al.*, Python Materials Genomics (pymatgen): A robust, open-source python library for materials analysis. *Computational Materials Science* **68**, 314-319 (2013).
53. D. Sheppard, P. Xiao, W. Chemelewski, D. D. Johnson, G. Henkelman, A generalized solid-state nudged elastic band method. *The Journal of chemical physics* **136**, (2012).
54. K. Han *et al.*, Narrow-Band Green-Emitting Hybrid Organic-Inorganic Eu (II)-Iodides for Next-Generation Micro-LED Displays. *Adv Mater* **36**, e2313247 (2024).
55. W. Chen, Y. Wang, G. Liu, C. Li, Z. Xia, Phosphor-in-Ceramic-Converted Laser-Driven Near-Infrared Light Sources for Multiple Intelligent Spectroscopy Applications. *Adv Mater* **36**, e2413857 (2024).
56. G. Zheng *et al.*, Glass-Crystallized Luminescence Translucent Ceramics toward High-Performance Broadband NIR LEDs. *Adv Sci (Weinh)* **9**, e2105713 (2022).
57. J. Qiao *et al.*, Near-Infrared Light-Emitting Diodes utilizing a Europium-Activated Calcium Oxide Phosphor with External Quantum Efficiency of up to 54.7%. *Adv Mater* **34**, e2201887 (2022).
58. Z. Jia *et al.*, Strategies to approach high performance in Cr^{3+}-doped phosphors for high-power NIR-LED light sources. *Light Sci Appl* **9**, 86 (2020).
59. S. Liu *et al.*, Site engineering strategy toward enhanced luminescence thermostability of a Cr^{3+}-doped broadband NIR phosphor and its application. *Materials Chemistry Frontiers* **5**, 3841-3849 (2021).
60. F. He *et al.*, A General Ammonium Salt Assisted Synthesis Strategy for Cr^{3+}-Doped Hexafluorides with Highly Efficient Near Infrared Emissions. *Advanced Functional Materials* **31**, 2103743 (2021).
61. J. Du, S. Liu, Z. Song, Q. Liu, All-Inorganic Green Synthesis of Small-Sized and Efficient $K_2SiF_6:Mn^{4+}$ Phosphor for Mini-LED Displays. *ACS Appl Mater Interfaces* **15**, 53738-53745 (2023).
62. Z. Hou *et al.*, A green synthetic route to the highly efficient $K_2SiF_6:Mn^{4+}$narrow-band red phosphor for warm white light-emitting diodes. *Journal of Materials Chemistry C* **6**, 2741-2746 (2018).
63. N. Hirosaki *et al.*, Characterization and properties of green-emitting β-SiAlON: Eu^{2+} powder phosphors for white light-emitting diodes. *Applied Physics Letters* **86**, 211905 (2005).

64. X. Zhang *et al.*, Controlling of Structural Ordering and Rigidity of β-SiAlON:Eu through Chemical Cosubstitution to Approach Narrow-Band-Emission for Light-Emitting Diodes Application. *Chemistry of Materials* **29**, 6781-6792 (2017).
65. D. Hu *et al.*, Ultra-Narrowband Green-Emitting Transparent Composite Ceramics for Laser-Driven Display. *Adv Mater* **37**, e2414957 (2025).
66. F. Galeotti, W. Mróz, M. Catellani, B. Kutrzeba-Kotowska, E. Kozma, Tailorable perylene-loaded fluorescent nanostructures: a multifaceted approach enabling their application in white hybrid LEDs. *Journal of Materials Chemistry C* **4**, 5407-5415 (2016).
67. N. J. Findlay *et al.*, An organic down-converting material for white-light emission from hybrid LEDs. *Adv Mater* **26**, 7290-7294 (2014).
68. S. C. Dong, Y. Jiang, C. W. Tang, Organic color-conversion media for full-color micro-LED displays. *Journal of the Society for Information Display* **29**, 961-967 (2021).
69. A. Aires, V. Fernandez-Luna, J. Fernandez-Cestau, R. D. Costa, A. L. Cortajarena, White-emitting Protein-Metal Nanocluster Phosphors for Highly Performing Biohybrid Light-Emitting Diodes. *Nano Lett* **20**, 2710-2716 (2020).
70. Z. Wu *et al.*, Assembly-Induced Enhancement of Cu Nanoclusters Luminescence with Mechanochromic Property. *J Am Chem Soc* **137**, 12906-12913 (2015).
71. Z. Wang *et al.*, All-Copper Nanocluster Based Down-Conversion White Light-Emitting Devices. *Adv Sci (Weinh)* **3**, 1600182 (2016).
72. L. Ai *et al.*, Engineering a red emission of copper nanocluster self-assembly architectures by employing aromatic thiols as capping ligands. *Nanoscale* **9**, 12618-12627 (2017).
73. D. Mosconi *et al.*, Synthesis and photochemical applications of processable polymers enclosing photoluminescent carbon quantum dots. *ACS nano* **9**, 4156-4164 (2015).
74. Z. Wang *et al.*, 53% Efficient Red Emissive Carbon Quantum Dots for High Color Rendering and Stable Warm White-Light-Emitting Diodes. *Adv Mater* **29**, 1702910 (2017).
75. T. Feng *et al.*, Color-Tunable Carbon Dots Possessing Solid-State Emission for Full-Color Light-Emitting Diodes Applications. *ACS Photonics* **5**, 502-510 (2017).
76. R. Guo, T. Li, S. Shi, Aggregation-induced emission enhancement of carbon quantum dots and applications in light emitting devices. *Journal of Materials Chemistry C* **7**, 5148-5154 (2019).
77. X. Zhang *et al.*, Highly fluorescent nitrogen-doped carbon dots with large Stokes shifts. *Journal of Materials Chemistry C* **11**, 11476-11485 (2023).
78. B. Karadza *et al.*, Bridging the Green Gap: Monochromatic InP-Based Quantum-Dot-on-Chip LEDs with over 50% Color Conversion Efficiency. *Nano Lett* **23**, 5490-5496 (2023).
79. H. Park *et al.*, Efficient Quantum Dot Color Conversion Layer with Mixed Spherical/Rod-Shaped Scattering Particles. *ACS Applied Optical Materials* **1**, 289-297 (2023).
80. B. R. Hyun *et al.*, Dual Role of Quantum Dots as Color Conversion Layer and Suppression of Input Light for Full-Color Micro-LED Displays. *J Phys Chem Lett* **12**, 6946-6954 (2021).
81. K.-L. Liang *et al.*, Highly Efficient Fine-Pitch Quantum Dot/Titanium Oxide Nanocomposites for Ultrahigh-Resolution Full-Color Micro-Light Emitting Diode Displays. *ACS Photonics* **11**, 2981-2991 (2024).
82. J. Lin *et al.*, Ultra-Stable Yellow Monolithic Perovskite Quantum Dots Film for Backlit Display. *Advanced Functional Materials* **34**, 2314795 (2024).
83. Z. Chen *et al.*, Tunable Green Light-Emitting $CsPbBr_3$ Based Perovskite-Nanocrystals-in-Glass Flexible Film Enables Production of Stable Backlight Display. *J Phys Chem Lett* **13**, 4701-4709 (2022).

84. R. Cheng *et al.*, Fibrous Nanoreactors from Microfluidic Blow Spinning for Mass Production of Highly Stable Ligand-Free Perovskite Quantum Dots. *Angew Chem Int Ed Engl* **61**, e202204371 (2022).
85. Q. Zhou *et al.*, In Situ Fabrication of Halide Perovskite Nanocrystal-Embedded Polymer Composite Films with Enhanced Photoluminescence for Display Backlights. *Adv Mater* **28**, 9163-9168 (2016).
86. H. Zhou *et al.*, Water Passivation of Perovskite Nanocrystals Enables Air-Stable Intrinsically Stretchable Color-Conversion Layers for Stretchable Displays. *Adv Mater* **32**, e2001989 (2020).
87. G. Liu *et al.*, Flexible, Stretchable, and Luminescent Hydrogels Based on a Polydimethylsiloxane-Coated $CsPbBr_3$ Nanostructure for Elastomers. *ACS Applied Nano Materials* **6**, 9588-9597 (2023).
88. J. Huang *et al.*, Monolithic Integration of Full-Color Microdisplay Screen with Sub-5 microm Quantum-Dot Pixels. *Adv Mater* **36**, e2409025 (2024).
89. J. I. Kim *et al.*, Strategies to extend the lifetime of perovskite downconversion films for display applications. *Advanced Materials* **35**, 2209784 (2023).
90. S. Wang *et al.*, Boosting Stability and Inkjet Printability of Pure-Red $CsPb(Br/I)_3$ Quantum Dots through Dual-Shell Encapsulation for Micro-LED Displays. *ACS Energy Letters* **9**, 2517-2526 (2024).
91. S. Chen *et al.*, Atomic-Scale Polarization and Strain at the Surface of Lead Halide Perovskite Nanocrystals. *Nano Lett* **23**, 6002-6009 (2023).
92. T. Bernards, M. Van Bommel, A. Boonstra, Hydrolysis-condensation processes of the tetra-alkoxysilanes TPOS, TEOS and TMOS in some alcoholic solvents. *Journal of non-crystalline solids* **134**, 1-13 (1991).
93. J. N. Yang *et al.*, Potassium Bromide Surface Passivation on CsPbI(3-x)Br(x) Nanocrystals for Efficient and Stable Pure Red Perovskite Light-Emitting Diodes. *J Am Chem Soc* **142**, 2956-2967 (2020).
94. T. Schmidt, K. Lischka, W. Zulehner, Excitation-power dependence of the near-band-edge photoluminescence of semiconductors. *Phys Rev B Condens Matter* **45**, 8989-8994 (1992).
95. M. Kaiser *et al.*, Interpreting the Time-Resolved Photoluminescence of Quasi-2D Perovskites. *Advanced Materials Interfaces* **8**, 2101326 (2021).
96. X. Zhang *et al.*, Enhancing the brightness of cesium lead halide perovskite nanocrystal based green light-emitting devices through the interface engineering with perfluorinated ionomer. *Nano letters* **16**, 1415-1420 (2016).
97. X. Zhang *et al.*, Bright Perovskite Nanocrystal Films for Efficient Light-Emitting Devices. *J Phys Chem Lett* **7**, 4602-4610 (2016).
98. H. Xu *et al.*, Exploring Orbit-Orbit Interaction in Relationship to Photoluminescence Quantum Efficiency in Perovskite Quantum Dots through Rashba Effect. *J Phys Chem Lett* **11**, 1-6 (2020).
99. H. W. Duan *et al.*, Bi-Ligand Synergy Enables Threshold Low Voltage and Bandgap Stable Pure-Red Mix-Halide Perovskite LEDs. *Advanced Functional Materials* **34**, 2310697 (2024).
100. P. Zeng *et al.*, Control of Hot Carrier Relaxation in $CsPbBr_3$ Nanocrystals Using Damping Ligands. *Angew Chem Int Ed Engl* **61**, e202111443 (2022).
101. K. Wei *et al.*, Temperature-dependent excitonic photoluminescence excited by two-photon absorption in perovskite $CsPbBr_3$ quantum dots. *Opt Lett* **41**, 3821-3824 (2016).
102. G. Mannino *et al.*, Temperature-Dependent Optical Band Gap in $CsPbBr_3$, $MAPbBr_3$, and $FAPbBr_3$ Single Crystals. *J Phys Chem Lett* **11**, 2490-2496 (2020).
103. J.-L. Song, C.-L. Hu, X. Xu, F. Kong, J.-G. Mao, Synthesis, crystal structures and properties of lead phosphite compounds. *Journal of Solid State Chemistry* **231**, 198-203 (2015).
104. H. Zhang *et al.*, Phase segregation due to ion migration in all-inorganic mixed-halide perovskite nanocrystals. *Nature communications* **10**, 1088 (2019).

105. L. A. Muscarella *et al.*, Which Ion Dominates the Temperature and Pressure Response of Halide Perovskites and Elpasolites? *J Phys Chem Lett* **14**, 9042-9051 (2023).
106. S.-J. Woo, J. S. Kim, T.-W. Lee, Characterization of stability and challenges to improve lifetime in perovskite LEDs. *Nature Photonics* **15**, 630-634 (2021).
107. T. Yamada, Y. Yamada, Y. Nakaike, A. Wakamiya, Y. Kanemitsu, Photon Emission and Reabsorption Processes in $CH_3NH_3PbBr_3$ Single Crystals Revealed by Time-Resolved Two-Photon-Excitation Photoluminescence Microscopy. *Physical Review Applied* **7**, 014001 (2017).
108. C. Liu *et al.*, Bulk $CsPb(Cl/Br)_3$ perovskite nanocrystals/polystyrene nanocomposites with controlled Rayleigh scattering for light guide plate. *Light Sci Appl* **12**, 261 (2023).
109. Y. Yin *et al.*, Full-Color Micro-LED Display with $CsPbBr_3$ Perovskite and CdSe Quantum Dots as Color Conversion Layers. *Advanced Materials Technologies* **5**, 2000251 (2020).
110. A. Zampetti, A. Minotto, F. Cacialli, Near-infrared (NIR) organic light-emitting diodes (OLEDs): challenges and opportunities. *Advanced Functional Materials* **29**, 1807623 (2019).
111. Y. Xiao *et al.*, NIR TADF emitters and OLEDs: challenges, progress, and perspectives. *Chemical Science* **13**, 8906-8923 (2022).
112. T. Yokota *et al.*, Ultraflexible organic photonic skin. *Science advances* **2**, e1501856 (2016).
113. H. Lee *et al.*, Toward all-day wearable health monitoring: An ultralow-power, reflective organic pulse oximetry sensing patch. *Science advances* **4**, eaas9530 (2018).

Acknowledgments:

Funding:

This research was supported by the Pioneer Research Center Program through the National Research Foundation of Korea (NRF) funded by the Ministry of Science, ICT & Future Planning (RS202500560490, RS202400422607, RS202400423271, RS202400425883, 2022M3H4A1A04096380). Q.Z. acknowledges support from Research Institute of Advanced Materials (RIAM). X.W.C. thanks the Agency for Science, Technology and Research (A*STAR, Singapore) for the National Science Scholarship. B.A.I.L. acknowledges the Engineering and Physical Sciences Research Council (EPSRC) and Cambridge Trusts for a PhD studentship. L.D. acknowledges UKRI guarantee funding for Marie Sklodowska-Curie Actions Postdoctoral Fellowships 2022 (EP/Y029429/1). S.D.S. acknowledges the Royal Society and Tata Group (grant no. UF150033, URF\R\221026). M.F. and H.J.B acknowledge funding from the European Union Horizon 2021 research and innovation programme (grant agreement No. 101073045 – TADF solutions).

Author contributions:
Conceptualization: QZ, TWL
Methods: QZ, YZ, HZ, TWL
Investigation: QZ, YZ, SP, HZ, HJS, TL, JR, MJS, XWC, EY, BAIL, SJW, MF, MJK, EAK, LD, JJ, YT, JJK, HC, KYJ, DHK, WJJ, JSK, HL, KL, SYC, CBP, SKL, MK, HJB, BH, AW, SDS, TWL
Visualization: QZ, YZ, JR
Funding acquisition: QZ, HJB, SDS, TWL
Writing – original draft: QZ
Writing – review & editing: QZ, TWL
All authors reviewed and commented on the manuscript.

Competing interests: Authors declare that they have no competing interests. The authors have filed related patent applications (Korean, PCT and US patent) based on the findings reported in this work.

Data and materials availability: All data and details of the synthesis of materials are available in the main text or the supplementary materials.

Supplementary Materials
Materials and methods

Fig. S1 to S56

Table S1 to S16

Supplementary notes 1 to 11

References (40 to 113)
Other Supplementary Material for this manuscript includes the following:

Movie S1 to S5